# Engineering Pyrite-Type Bimetallic Ni-Doped CoS$_2$ Nanoneedle Arrays over a Wide Compositional Range for Enhanced Oxygen and Hydrogen Electrocatalysis with Flexible Property

**Guowei He [1], Wei Zhang [1], Yida Deng [1], Cheng Zhong [1,2], Wenbin Hu [1,2] and Xiaopeng Han [1,2,3,*]** ID

[1] Tianjin Key Laboratory of Composite and Functional Materials, School of Materials Science and Engineering, Tianjin University, Tianjin 300072, China; guowei_he@tju.edu.cn (G.H.); dazhangwei@tju.edu.cn (W.Z.); yida.deng@tju.edu.cn (Y.D.); cheng.zhong@tju.edu.cn (C.Z.); wbhu@tju.edu.cn (W.H.)

[2] Key Laboratory of Advanced Ceramics and Machining Technology (Ministry of Education), Tianjin University, Tianjin 300072, China

[3] Key Laboratory of Advanced Energy Materials Chemistry (Ministry of Education), Nankai University, Tianjin 300071, China

\* Correspondence: xphan@tju.edu.cn; Tel.: +86-22-2740-5368

**Abstract:** The development of cheap and efficient catalytic electrodes is of great importance, to promote the sluggish overall water-splitting systems associated with the large-scale application of clean and renewable energy technologies. In this work, we report the controlled synthesis of pyrite-type bimetallic Ni-doped CoS$_2$ nanoneedle (NN) arrays supported on stainless steel (SS) (designated as Ni$_x$Co$_{1-x}$S$_2$ NN/SS, $0 \leq x \leq 1$) and the related compositional influence on electrocatalytic efficiencies for the oxygen and hydrogen evolution reaction (OER/HER). Impressively, the Ni$_{0.33}$Co$_{0.67}$S$_2$ NN/SS displays superior activity and faster kinetics for catalyzing OER (low overpotential of 286 mV at 50 mA cm$^{-2}$; Tafel value of 55 mV dec$^{-1}$) and HER (low overpotential of 350 mV at 30 mA cm$^{-2}$; Tafel value of 76 mV dec$^{-1}$) than those of counterparts with other Ni/Co ratios and also monometallic Ni- or Co-based sulfides, which is attributed to the optimized balance from the improved electron transfer capability, increased exposure of electrocatalytic active sites, and favorable dissipation of gaseous products over the nanoneedle surface. Furthermore, the conductive, flexible SS support and firmly attached in-situ integrated feature, result in the flexibility and remarkable long-term stability of as-prepared binder-free Ni$_{0.33}$Co$_{0.67}$S$_2$ NN/SS electrode. These results demonstrate element-doping could be an efficient route at the atomic level to design new materials and further optimize the surface physicochemical properties for enhancing the overall electrochemical water splitting activity.

**Keywords:** nanoneedle; nickel cobalt sulfide; element-doping; electrocatalysis; flexible; water splitting

## 1. Introduction

As an ideal alternative, hydrogen production from electrochemical or photo-electrochemical water splitting represents one of the most promising strategies to relieve the tension of the growing crisis from energy and environmental concerns [1,2]. Typically, water splitting involves two half reactions (i.e., the hydrogen evolution reaction (HER) and oxygen evolution reaction (OER)), both of which are kinetically sluggish in nature [3]. Thus, highly efficient catalysts are required to promote the slow reaction kinetics, affording a high evolution current at low dynamic overpotentials [4]. Currently, Pt and IrO$_2$/RuO$_2$ are recognized as state-of-art electrocatalysts for accelerating HER

and OER processes, respectively. Unfortunately, the limited natural reserves and exorbitant price of these precious metal elements seriously hinders their widespread applicability in commercial electrolyzers [4,5]. Furthermore, developing a bifunctional electrocatalyst, that is capable of catalyzing dual HER and OER, is of great interest, as it could potentially simplify the electrolyzer structures and substantially reduce the device cost. However, despite using the noble metals, Pt is basically active towards only HER, while $IrO_2$ or $RuO_2$ possesses superior activity for only OER [6,7]; thus, it remains a big challenge to simultaneously achieve the satisfied HER and OER capabilities within the same electrocatalyst. Therefore, in this context, it is extremely urgent to search earth-abundant and bi-active electrocatalysts to expedite HER and OER kinetics, to construct the next generation of water-splitting technologies.

Over the past decades, various electrocatalysts have been designed and extensively investigated to replace precious metals, including transition metal carbides [8–10], nitrides [11,12], sulfides [13–16], selenides [17,18], phosphides [19–21] as well as their nanocomposites [22–24] for HER, and transition metals [25–28], hydroxides [29–31], oxides [32–34], and phosphates [20,35] for OER. Among them, the pyrite-type transition metal dichalcogenides ($MX_2$, M = Fe, Co, Ni and X = S, Se) have recently attracted growing research interest because of their extremely earth abundance, environmental benign, and satisfied long-term durability in either acidic or alkaline environments [13–18]. In particular, cobalt pyrite disulfide ($CoS_2$) exhibits an intrinsically conductive metallic property, in contrast to the semi-conducting pyrites [36], such as nickel and iron disulfides, making it highly attractive as an electrode material for energy storage and conversion applications. As for catalyzing HER and OER, numerous strategies have been developed to further enhance the electrocatalytic performance, to reach a specified level through nanostructuring, for example, by decreasing particle size and increasing the number of available catalytic sites [28,34], integrating with a conducting substrate by facilitating both charge and carrier transport [10,32,37] or constructing hetero-structures with other metal oxides or sulfides by tuning the surface electronic structure and synergistic interaction [24,38]. Metal and non-metal substituting has been proved to be a facile and efficient route to engineer the surface atomic configuration and multi-functional redox sites, thus optimizing the intrinsic electrochemical behaviors [39–41]. For example, $NiCo_2S_4$@graphene demonstrates superior overall bifunctional oxygen electrocatalytic activities, compared to Ni-free $Co_3S_4$@graphene [40]; Jin's group developed a ternary pyrite-phase cobalt phosphosulphide to improve HER activity by modifying the electronic structure, and further, the hydrogen adsorption energy, on the surface active sites [19]. Recently, doping Ni into $CoS_2$ to form bimetallic Ni-Co sulphides with pyrite-type structures, displays superior pseudocapacitance, compared to monometallic Co and Ni sulphides, owing to the combined contributions from surface-exposed Ni and Co active species [42,43]. Meanwhile, HER and OER performance can also be dramatically influenced by the composition of nickel cobalt sulphides, e.g., the Ni-doping fraction in the final composite. As for application in HER, Cui et al. have demonstrated that after merging with 10% Ni, the bimetal catalyst ($Ni_{0.1}Co_{0.9}S_2$) shows remarkable catalytic activity, which is superior to bare $CoS_2$ and other benchmarks ($Ni_{0.05}Co_{0.95}S_2$ and $Ni_{0.2}Co_{0.8}S_2$) [44]. In contrast, Kong et al. and Faber et al. both revealed that doping a certain amount of Ni into $CoS_2$ would have a negative effect on improving the HER activity, for example, $Ni_{0.68}Co_{0.32}S_2$ and $Ni_{0.41}Co_{0.59}S_2$ exhibit inferior performances than their counterpart, $CoS_2$ [14,45]. It seems that ambiguous results exist concerning the effect of Ni on tuning the electrocatalytic activities of pyrite $CoS_2$ nanostructures. Therefore, it is highly essential to perform a systematic study over a wide compositional range of metal-doping, to gain a deeper understanding about the foreign atomic effect on material properties and further optimize their hydrogen and oxygen electrocatalytic behaviors.

In this paper, which is aimed at elucidating the relationship between the Ni concentration doping into the $CoS_2$ matrix and their catalytic capabilities, we present herein the preparation of a series of Ni-doped $CoS_2$ multi-level nanoneedle (NN) arrays on stainless steel (SS) (designated as $Ni_xCo_{1-x}S_2$ NN/SS) and the systematical comparison of their electrocatalytic properties in alkaline electrolyte. The synthesis is achieved via a general two-step hydrothermal method, whereas Ni–Co

carbonate hydroxide precursors were firstly in-situ grown on a SS support and then transformed into corresponding Ni–Co sulfides. Interestingly, the electrocatalytic performance of $Ni_xCo_{1-x}S_2$ series was optimized at a Ni/Co molar ratio of 1:2 ($Ni_{0.33}Co_{0.67}S_2$, $x = 0.33$) over a wide compositional range ($0 \leq x \leq 1$), which exhibits superior HER and OER efficiencies, compared to other counterparts of $Ni_{0.5}Co_{0.5}S_2$ ($x = 0.5$) and $Ni_{0.67}Co_{0.33}S_2$ ($x = 0.67$) as well as monometallic $CoS_2$ and $NiS_2$. In particular, the onset potential where OER occurs on $Ni_{0.33}Co_{0.67}S_2$ NN/SS is as low as 245 mV, and the required overpotential is 286 mV to deliver an OER current density of 50 mA $cm^{-2}$, which outperforms the reported state-of-art OER electrocatalysts. Furthermore, benefiting from the in-situ integrated feature on SS mesh, the resulting carbon- and binder-free $Ni_{0.33}Co_{0.67}S_2$ NN/SS electrode also renders remarkable flexibility and considerable long-term catalytic durability. Extensive analyses have demonstrated that the superior activity is attributed to a subtle balance between the electronic conductivity, the energetically modified active sites, and the favorable release of generated gaseous products over the nanoneedle surface, which simultaneously facilitates the electron, ion, gas transfer and the chemisorptions of hydrogen and oxygen-containing species, consequently enhancing the overall water oxidation activity.

## 2. Results and Discussion

### 2.1. Synthesis and Characterization

A general two-step hydrothermal method was developed to synthesize the $Ni_xCo_{1-x}S_2$ nanoneedle arrays on the SS substrate, whereas Ni–Co carbonate hydroxide precursor was grown in the first step and then transformed into corresponding Ni–Co sulfides after the second sulfidation treatment (Figure 1a). The phase conversion was also evidenced by the color change of the samples covering the SS surface. The Ni/Co ratios can be easily tuned by controlling the addition of Ni and Co-contained resources. The crystallographic information of as-prepared samples was analyzed by powder X-ray diffraction (XRD). As depicted in Figure 1b, the diffraction peaks of the Ni–Co precursor can be well matched with the combination of standard peaks of $Co(CO_3)_{0.5}OH$ (JCPDS card no. 48-0083) and $Ni(CO_3)_{0.5}OH$ (JCPDS card no. 35-0501). The Ni–Co-carbonate hydroxides with different Ni/Co ratios were completely converted into corresponding pyrite-type Ni-doped $CoS_2$, via an anion exchange reaction in a sodium sulfide environment at 120 °C for 8 h (Figure 1c). During this step, the active sulfur anions replace the $CO_3^{2-}$ and $OH^-$ ions in the Ni–Co–carbonate hydroxides to form the $Ni_xCo_{1-x}S_2$ phase structure. All the identified diffraction peaks of prepared $Ni_xCo_{1-x}S_2$ at 2θ values of about 27°, 32°, 36°, 39°, 46°, 54°, 57°, 60°, 62° and 73° can be unambiguously indexed to (111), (200), (210), (211), (220), (311), (222), (230), (321) and (331) planes of cubic $CoS_2$ (JCPDS card no. 89-3056; space group: Pa-3; $a = b = c = 5.523$ Å), but are slightly shifted to lower angles, owing to the substitution of larger $Ni^{2+}$ ions ($r_{Ni}^{2+} = 0.069$ nm) for smaller $Co^{2+}$ ions ($r_{Co}^{2+} = 0.065$ nm) on the metal sites. The replacement of Ni to Co does not affect the crystal structure of $CoS_2$, even up to a maximum percentage of 100% ($Ni_xCo_{1-x}S_2$, $0 \leq x \leq 1$), owing to the similar physical and chemical properties of Ni and Co ions as well as their structural compatibility [46]. Noticeably, the 2θ values of the XRD diffraction peaks of pyrite-typed $Ni_xCo_{1-x}S_2$ are located between $CoS_2$ and $NiS_2$ (JCPDS card no. 73-0574, Table S1), further revealing the formation of an alloyed pyrite phase. No other signals of impurities have been detected, especially from the parent hydroxide, implying the complete conversion and high phase purity of as-prepared sulfides. Therefore, XRD results demonstrate the successful synthesis of the $Ni_xCo_{1-x}S_2$ series, with solid solubility over a wide compositional range of $0 \leq x \leq 1$ [39]. The same crystallographic phase is the primary reason, which accounts for the possible achievement of Ni-doped $CoS_2$. As shown in Figure 1d, the crystal structure is based on the framework of corner-sharing $MS_6$ octahedra in pyrite-type $MS_2$ (M = Ni or Co). The pyrite crystal structure of $CoS_2$ and $NiS_2$ thus ensures the successful substitution of $CoS_2$ by Ni ions, while still maintaining the cubic structural symmetry. The parallel formation of $Ni_xCo_{1-x}S_2$ compounds with the same crystal

symmetry allows us to focus on the investigation of compositional and surface active effects on their electrochemical properties.
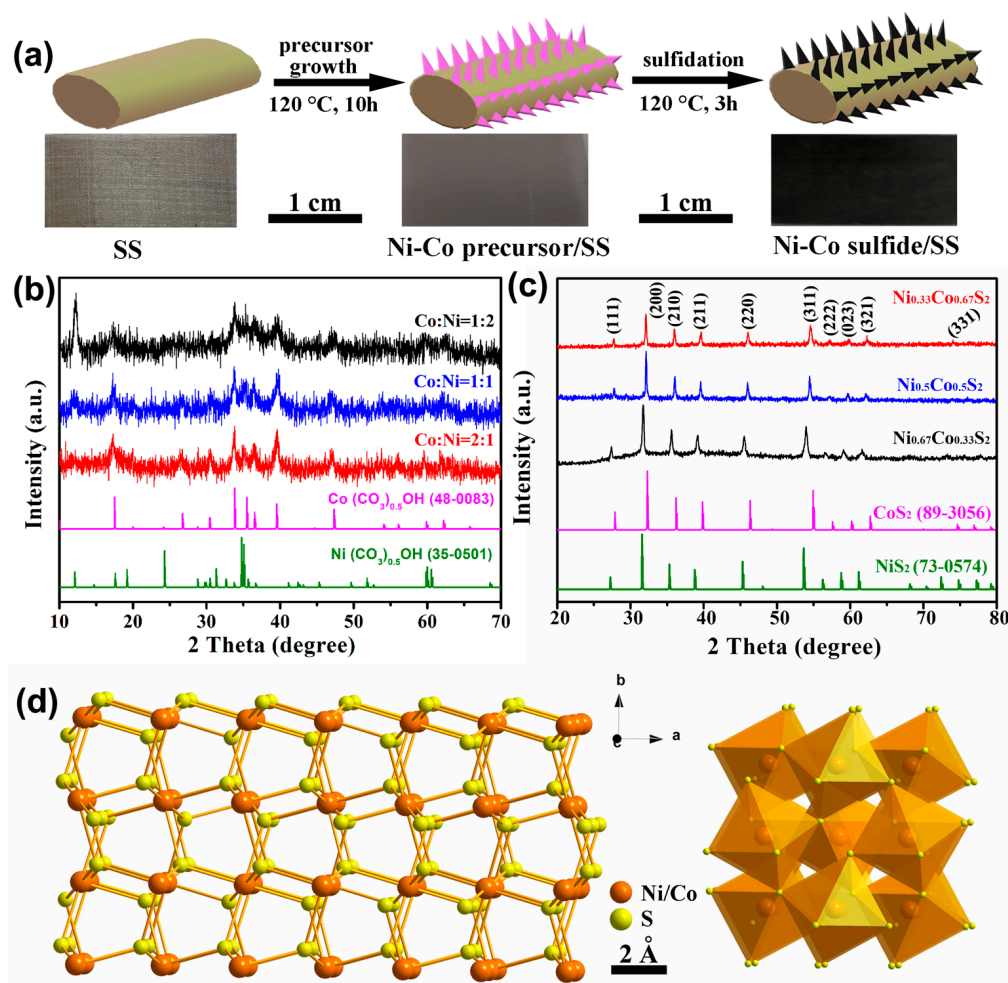


**Figure 1.** (**a**) Schematic illustration of the preparation procedures of $Ni_xCo_{1-x}S_2$ NN/SS and the corresponding electrode photographs; (**b**) XRD patterns of Ni–Co composite precursors and (**c**) final $Ni_xCo_{1-x}S_2$ with Ni/Co ratios of 1:2, 1:1, and 2:1, respectively. The standard peaks of $CoS_2$ and $NiS_2$ are also shown for comparison; (**d**) Crystal structures of pyrite-type $Ni_xCo_{1-x}S_2$.

The micro-nanostructures and morphologies of prepared Ni–Co precursors and sulfides were characterized by scanning electron microscopy (SEM) and transmission electron microscopy (TEM) techniques. From the SEM images of the prepared Ni–Co carbonate hydroxide precursors, we can see that the products have high similarity in microstructure despite different molar ratios of Ni to Co in their components (Figure 2a–c), while completely different morphologies are obtained for pure $Co(CO_3)_{0.5}OH$ and $Ni(CO_3)_{0.5}OH$ (Figure S1). Specifically, the SS substrate is covered densely and uniformly by the Ni–Co precursor nanoneedle arrays on a larger scale size (Figure S2), whereas nanoflake and nanowire-aggregated products are formed in the presence of only $Co^{2+}$ or $Ni^{2+}$ ions (Figure S1). Moreover, as the Ni-doping content increases in Ni–Co precursors, the corresponding nanoneedle becomes shorter, narrower and rougher (Figure 2a–c), which can be attributed to the doping effect on the size control of nanocrystals [47]. This is also echoed with previous phenomena, namely, the grain sizes slightly decreased with an increasing concentration of metallic Ni element in Ni–Co-based nanocomposites [44,48]. After the sulfidation treatment, the nanoneedle arrays were well-retained in the final $Ni_xCo_{1-x}S_2$, with the appearance of porous nanostructures and increased surface roughness (Figure 2d–f). Additionally, in contrast to the energy dispersive spectroscopy (EDS)

of the precursor, containing Ni, Co, and O (Figure S3), the EDS results of the as-prepared sulfide disclosed the presence of Ni, Co and S elements in the final $Ni_xCo_{1-x}S_2$ products (Figure 2g–i), again verifying the successful phase conversion from the Ni–Co carbonate hydroxide precursor to Ni–Co sulfide after the hydrothermal sulfidation treatment. Moreover, the detected Ni/Co molar ratios in fabricated $Ni_{0.33}Co_{0.67}S_2$, $Ni_{0.5}Co_{0.5}S_2$, and $Ni_{0.67}Co_{0.33}S_2$ nanoneedles were about 1:1.98, 1:0.80, and 2.22:1, respectively. The slightly difference relative to the ideal ratios (i.e., 1:2, 1:1, and 2:1) is mainly ascribed to the different reaction activities of Ni and Co cations during the phase formation process [49].
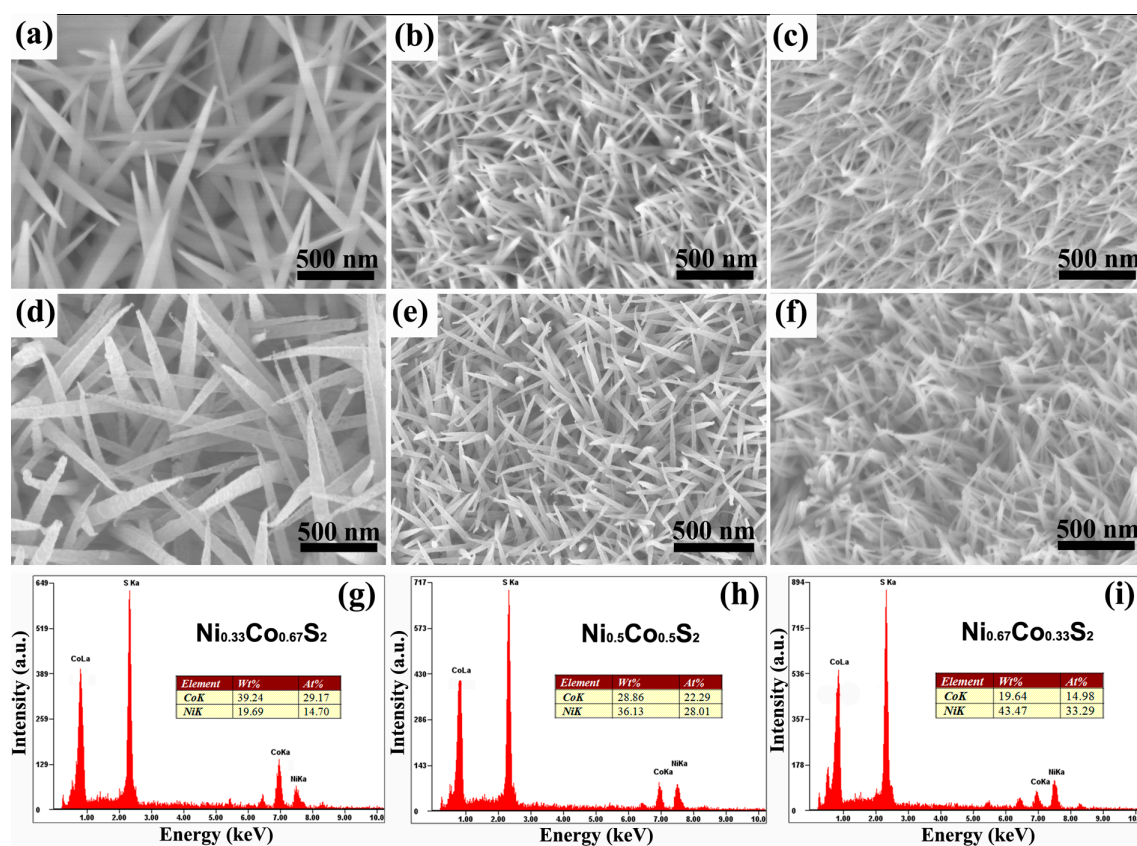


**Figure 2.** SEM images of the as-synthesized Ni–Co precursors (**a**–**c**), $Ni_xCo_{1-x}S_2$ (**d**–**f**) and EDS spectra. The corresponding Ni/Co molar ratios were 1:2 (**a**,**d**,**g**), 1:1 (**b**,**e**,**h**), and 2:1 (**c**,**f**,**i**), respectively.

TEM was employed to further identify the micro-nanostructure and detailed structural information of as-synthesized samples. TEM images of samples detached from the stainless steel again suggested the morphological nanoneedle of both Ni–Co precursors and the final $Ni_{0.33}Co_{0.67}S_2$ sample (Figure 3), in accordance with the SEM observation (Figure 2d). The surface feature of Ni–Co precursors is relatively smooth, with no obvious pore structures (Figure 3a). In the corresponding high-resolution TEM (HRTEM), the measured distance of 0.26 nm matches well with the (221) lattice plane of Ni–Co-carbonate hydroxide (Figure 3b), which is also supported by the ring patterns of selected area electron diffraction (SAED, inset in Figure 3b). After sulfidation, the surface texture became rough and porous nanostructure appeared (Figure 3c). The observed lattice fringe with a spacing of 0.32 nm can be assigned to the (111) facets of Ni-doped $CoS_2$ (Figure 3d), as can be gleaned from the SAED pattern (inset in Figure 3d). The measured interplanar distance was also confirmed by the intensity profiles from the selected areas of Figure 3b,d (Figure S4). The TEM analysis here further corroborated the phase conversion from the Ni–Co precursor to sulfide after the hydrothermal treatment. Similar results were also obtained from the TEM and HRTEM images of $Ni_{0.5}Co_{0.5}S_2$ and

$Ni_{0.67}Co_{0.33}S_2$ nanoneedle arrays (Figure S5), collectively testifying the above crystallographic and morphological information from the XRD and SEM analyses.
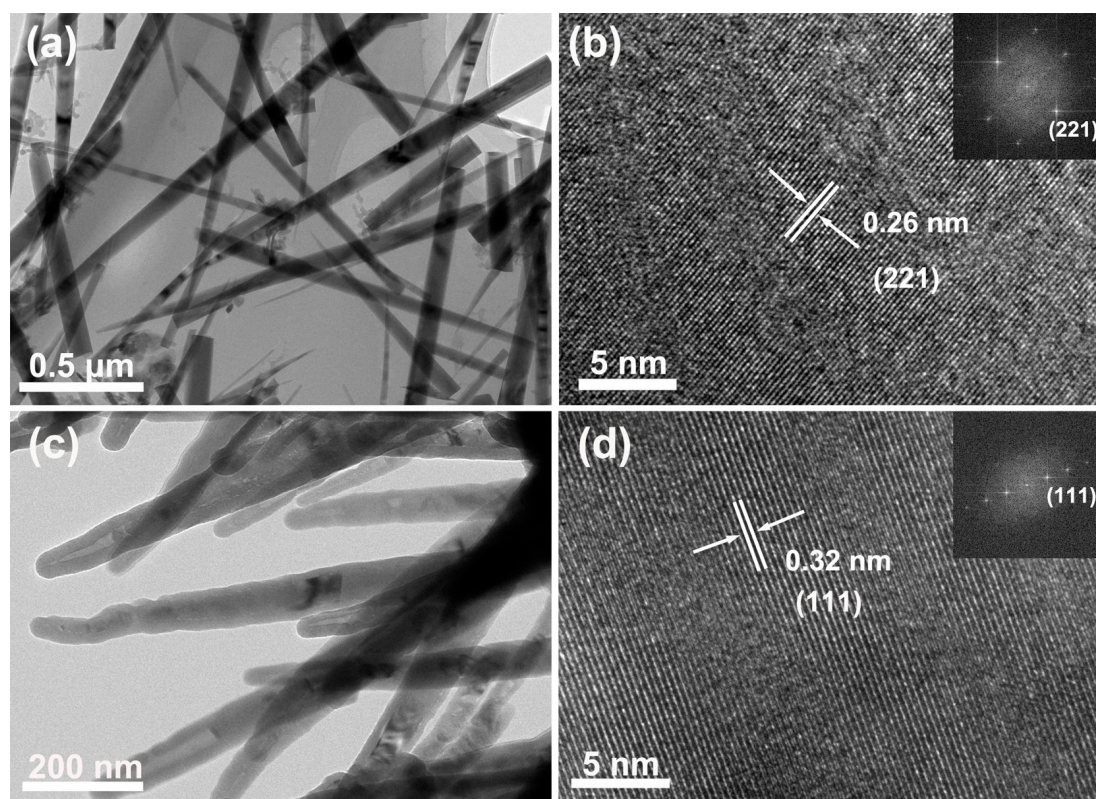


**Figure 3.** TEM and HRTEM images of the Ni–Co precursor (**a**,**b**) and final Ni-doped $CoS_2$ (**c**,**d**) with a Ni/Co molar ratio of 1:2.

X-ray photoelectron spectroscopy (XPS) was further performed, to characterize the elemental compositions and surface chemical valences of synthesized Ni-doped $CoS_2$ in the near-surface range. The XPS survey spectra of $Ni_{0.37}Co_{0.66}S_2$, in Figure 4a, reveals the presence of Ni, Co, and S elements with molar ratios of 1:2:6.7, consistent with theoretical values (1:2:6). The additional C (as a reference) and O elements are ascribed to exposure to air. The spin-orbit doublets and two shakeup satellites (denoted as "Sat.") can be well fitted in the Ni 2p high-resolution XPS spectra, by using a Gaussian fitting method (Figure 4b), which is respectively assigned to the characteristic peaks of $Ni^{2+}$ and $Ni^{3+}$. The Co 2p spectra (Figure 4c) can be de-convoluted into six species, including pairs of fitting peaks for $Co^{2+}$ and $Co^{3+}$, and their shakeup satellites. The Ni and Co 2p spectra reveal the coexistence of $Ni^{2+}/Ni^{3+}$ and $Co^{2+}/Co^{3+}$ in the prepared $Ni_{0.33}Co_{0.67}S_2$ product, in accordance with reported results in the literature [50]. The S 2p XPS peak of $Ni_{0.33}Co_{0.67}S_2$ NN can be assigned into four peaks (Figure 4d). Two peaks, located at 161.5 and 162.7 eV, correspond to S $2p_{1/2}$ and S $2p_{3/2}$ of $S^{2-}$, respectively. Another peak, centered at 164.2 eV, is the signal from bridging $S_2^{2-}$ [51], which has been recognized to facilitate the HER electrocatalysis [52]. The binding peak at 168.8 eV is ascribed to the shakeup satellite peak [53]. These XPS results together demonstrate the presence of $Ni^{2+}/Ni^{3+}$, $Co^{2+}/Co^{3+}$ and $S^{2-}/S_2^{2-}$ in the synthesized $Ni_xCo_{1-x}S_2$ nanostructures, well agree with those reported previously [50].

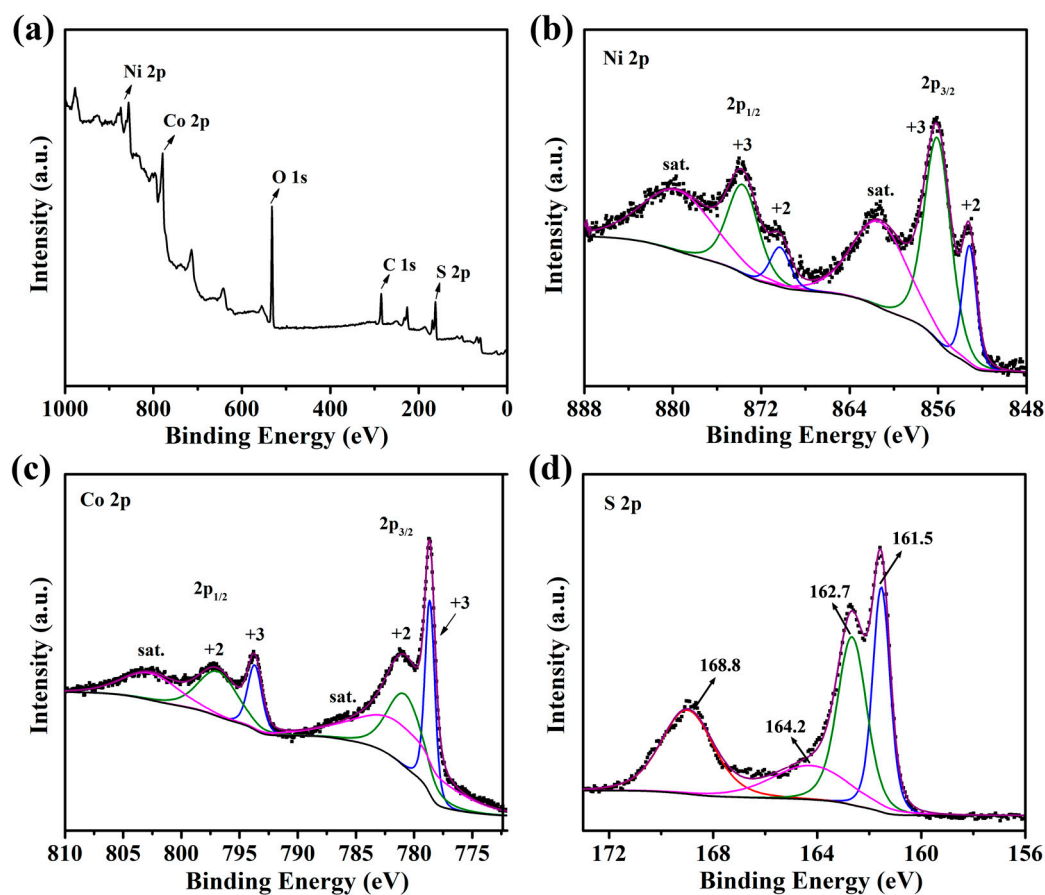**Figure 4.** (**a**) XPS survey spectra; (**b**) Ni 2p; (**c**) Co 2p; and (**d**) S 2p high-resolution spectra of $Ni_{0.37}Co_{0.66}S_2$ NN, respectively.

## 2.2. Electrocatalytic Performance

To investigate the electrocatalytic activities of the as-synthesized self-standing electrodes, electrochemical measurements were carried out in $N_2$-saturated 1.0 M KOH, using a three-electrode configuration (without *iR* correction for all the data). The prepared binder and conductive additive-free $Ni_xCo_{1-x}S_2$ NN/SS electrode, with catalyst loading around 1.2 mg cm$^{-2}$, was directly employed as a working electrode. Monometallic sulfides of $CoS_2$ and $NiS_2$ as well as precious metal $RuO_2$ were also evaluated as benchmarks for comparison. As revealed in the OER linear sweep voltammetry (LSV) curves (Figure 5a and Figure S6), the bimetallic $Ni_xCo_{1-x}S_2$ NN with different Ni/Co ratios exhibits superior water oxidation activity compared to monometallic $CoS_2$, $NiS_2$, and also the precious metal catalyst of $RuO_2$. Particularly, the $Ni_{0.33}Co_{0.67}S_2$ catalyst affords the best OER performance with the required overpotential (η) of 286 mV, to reach an evolution current density of 50 mA cm$^{-2}$, which is slightly lower than its $Ni_{0.5}Co_{0.5}S_2$ (292 mV) and $Ni_{0.67}Co_{0.33}S_2$ (297 mV) counterparts and also much lower than bare $CoS_2$ (340 mV), $NiS_2$ (420 mV) and $RuO_2$ (365 mV), respectively. The anodic peak near 1.36 V in the curves is ascribed to the Ni oxidation state from Ni(II) to Ni(III) [54]. The corresponding Tafel plots were fitted on the basis of the LSV polarization curves, as displayed in Figure 5b. The Tafel analysis reveals that a much smaller Tafel slope of 55 mV dec$^{-1}$ is fitted over the $Ni_{0.33}Co_{0.67}S_2$ surface than those on $Ni_{0.5}Co_{0.5}S_2$ (61 mV dec$^{-1}$) and $Ni_{0.67}Co_{0.33}S_2$ (68 mV dec$^{-1}$), indicative of the faster OER kinetic catalyzing by $Ni_{0.33}Co_{0.67}S_2$ nanoneedle arrays. Furthermore, in Tafel region, the linear relationship between logarithmic current density and overpotential extends a larger region of higher current density for $Ni_{0.33}Co_{0.67}S_2$ nanoneedles, fingering its lower mass transfer resistance at higher evolution currents [50]. Moreover, electrochemical impedance spectroscopy (EIS), under OER operating

conditions, was performed, to characterize the electrical conductivities and charge transport properties of synthesized electrocatalysts (Figure 5c). The fitted charge transfer resistance ($R_{ct}$) values are in good accordance with the trend of OER activities, further corroborating the faster catalytic kinetics in favoring the superior catalytic performance of $Ni_{0.33}Co_{0.67}S_2$ nanoneedles among the $Ni_xCo_{1-x}S_2$ series. Notably, the OER parameters of $RuO_2$ are comparable to the values reported in the literature and the presented performance of $Ni_{0.33}Co_{0.67}S_2$ NN/SS rivals those of the most active earth-abundant element-based electrocatalysts reported so far (see detailed comparison in Table S2).
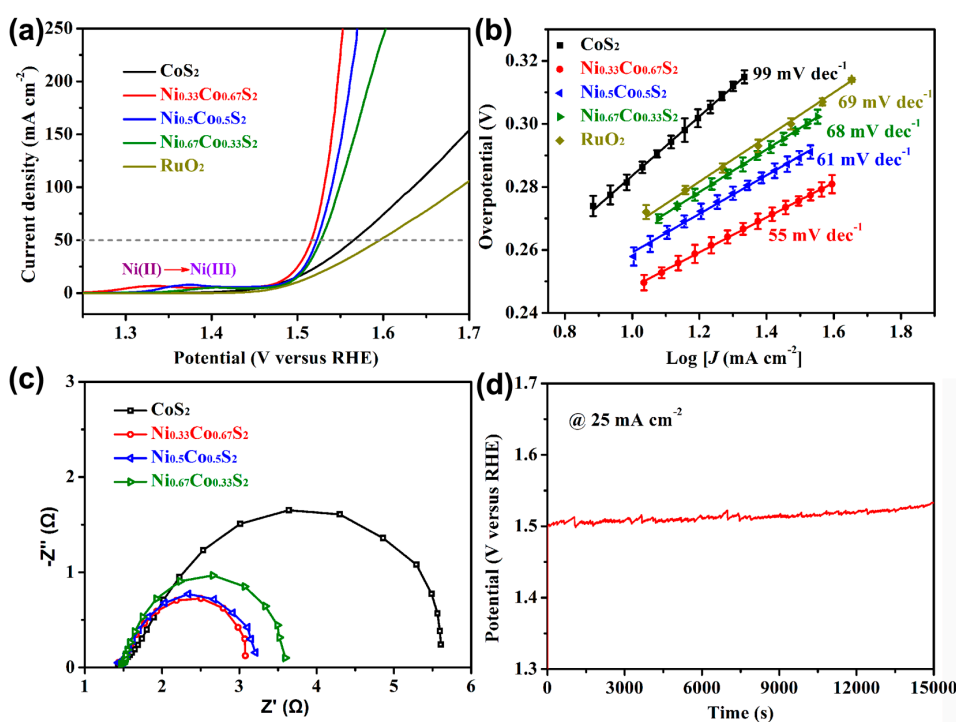


**Figure 5.** (**a**) Oxygen evolution reaction (OER) performance of commercial $RuO_2$, bare $CoS_2$ and Ni-doped $CoS_2$ nanoneedle arrays on SS in 1.0 M KOH. The scan rate is 5 mV s$^{-1}$; (**b**) Corresponding Tafel plots. The error bar stands for the results, ranging from three independent repeated measurements; (**c**) Nyquist plots of the four catalysts at an overpotential of 300 mV; (**d**) Chronopotentiometric response of $Ni_{0.33}Co_{0.67}S_2$ NN/SS at a constant anodic current density of 25 mA cm$^{-2}$.

Besides the catalytic activity, the $Ni_{0.33}Co_{0.67}S_2$ NN rooted on SS substrate also presented excellent OER electrochemical stability for continuous long-term OER processes (Figure 5d). At a fixed OER current density of 25 mA cm$^{-2}$, there was no obvious degradation of the overpotential of $Ni_{0.33}Co_{0.67}S_2$ NN/SS after an operation period of 15,000 s, suggesting the wonderful long-term catalytic durability. During our testing process, we observed that the evolved oxygen bubbles dissipated rapidly into the electrolyte with no big bubbles remaining on the electrode surface, which mainly contributes to the novel one-dimensional (1D) nanoneedle arrays, facilitating the gas and mass transfer and thus maintaining the effective solid–liquid interface for electrocatalysis [16,36]. This conjecture has been verified by the fact that the nanoneedle arrays were still essentially preserved after successive long-term OER electrolysis (Figure S7). Despite undergoing an increase of a typical size, the distributed nanoneedles were firmly attached onto the stainless steel without obvious aggregation and detachment, which is believed to be another pivotal factor to the structural durability and remarkable electrochemical robustness of $Ni_xCo_{1-x}S_2$ NN/SS electrode in alkaline conditions.

To explore the suitability of as-synthesized $Ni_xCo_{1-x}S_2$ NN/SS in the process of overall water-splitting, the HER activities were assessed using the same solution. As displayed in the HER polarization profiles of Figure 6a, the $Ni_{0.33}Co_{0.67}S_2$ NN/SS delivered a cathodic current

density of 30 mA cm$^{-2}$ at an overpotential of 350 mV, which is lower than that of comparative Ni$_{0.5}$Co$_{0.5}$S$_2$ (370 mV) and Ni$_{0.67}$Co$_{0.33}$S$_2$ (387 mV). Similar to the case for catalyzing OER, all the bimetallic Ni-doped CoS$_2$ electrodes exhibit lower overpotentials than those of un-doped CoS$_2$ and NiS$_2$ (Figure S8), an indication that the introduction of atomic Ni on the metal sites has a positive effect on enhancing hydrogen and oxygen electrocatalysis. Although the precious catalyst, Pt/C, afforded a current density of 30 mA cm$^{-2}$ at a very low overpotential of 200 mV, the prepared Ni$_{0.33}$Co$_{0.67}$S$_2$ NN/SS electrode transcended Pt/C at large current densities (>110 mA cm$^{-2}$), indicating the superior capability of the former in large-scale hydrogen evolution applications. Figure 6b gives the corresponding Tafel plots. The fitted Tafel slope of the Ni$_{0.33}$Co$_{0.67}$S$_2$ (76 mV dec$^{-1}$) was lower than those of Ni$_{0.5}$Co$_{0.5}$S$_2$ (82 mV dec$^{-1}$), Ni$_{0.67}$Co$_{0.33}$S$_2$ (89 mV dec$^{-1}$) and CoS$_2$ (98 mV dec$^{-1}$) counterparts, respectively. These Tafel values of Ni$_x$Co$_{1-x}$S$_2$ suggest that the HER proceeds the Volmer–Heyrovsky mechanism [38]. Moreover, the Tafel values are consistent with the HER performance trend, which further reveals that the HER kinetics follow an order of Ni$_{0.33}$Co$_{0.67}$S$_2$ > Ni$_{0.5}$Co$_{0.5}$S$_2$ > Ni$_{0.67}$Co$_{0.33}$S$_2$ > CoS$_2$.
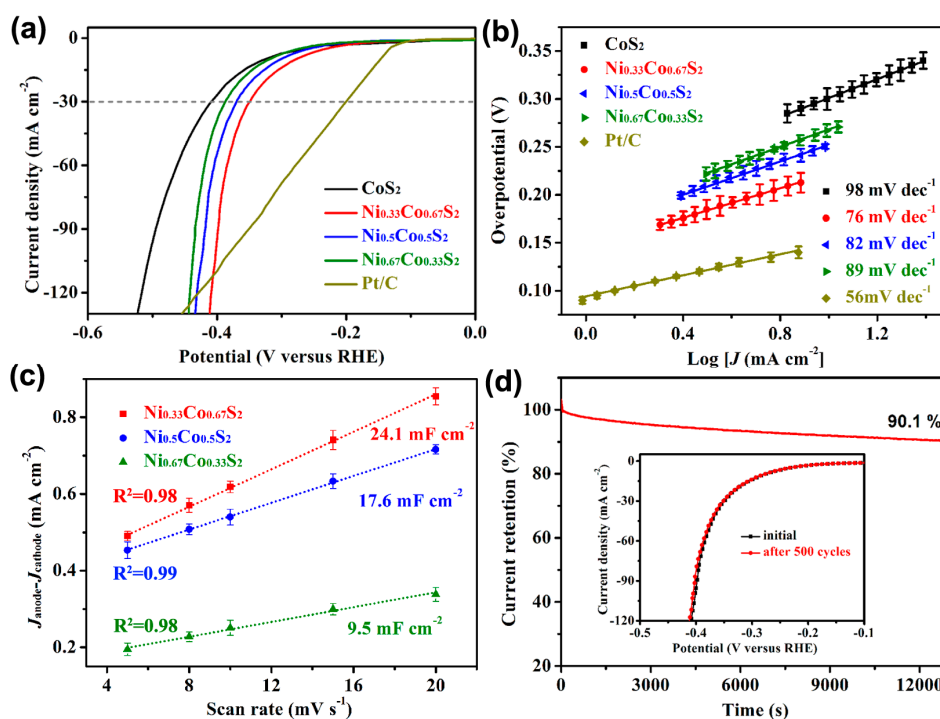


**Figure 6.** (**a**) HER polarization curves of commercial Pt/C, bare CoS$_2$ and Ni-doped CoS$_2$ on SS in 1.0 M KOH. The scan rate is 5 mV s$^{-1}$; (**b**) Fitted Tafel slopes; (**c**) Calculation of double-layer capacitance by fitting the capacitive current vs. scan rates. The error bar stands for the results, ranging from three independent repeated measurements; (**d**) Chronoamperometric data of Ni$_{0.33}$Co$_{0.67}$S$_2$ NN/SS at a constant potential of −0.35 V. Inset shows the polarization plots of first cycle and after 500 cycles.

It has been recognized that the HER catalytic activity is largely determined by the electrochemical active surface area (ECSA). To estimate the ECSA of these prepared Ni-doped CoS$_2$ catalysts, we measured the electric double layer capacitance (EDLC) at the electrode–electrolyte interface, by fitting the capacitive currents as a function of scan rates (Figure S9). Accordingly, the determined EDLC values of Ni$_{0.33}$Co$_{0.67}$S$_2$, Ni$_{0.5}$Co$_{0.5}$S$_2$, and Ni$_{0.67}$Co$_{0.33}$S$_2$ were ca. 24.1, 17.6, and 9.5 mF cm$^{-2}$ (Figure 6c), respectively, which demonstrates that the enhancement of the Ni$_{0.33}$Co$_{0.67}$S$_2$ sample in providing a higher active surface area and larger amount of active sites, as compared to the controlled samples with other Ni/Co ratios. Apart from the high activity, the catalytic durability is also required for constructing a proof-of-concept electrocatalyst. To assess the HER durability,

the $Ni_{0.33}Co_{0.67}S_2$ NN/SS electrode was cycled continuously for 500 potential cycles. No obvious activity decay was detected (Figure 6d), suggesting the considerable long-term stability for HER electrocatalysis below 0 V in alkaline electrolyte. Meanwhile, in the chronoamperometric measurement after 13,000 s, the $Ni_{0.33}Co_{0.67}S_2$ NN/SS electrode maintained 90.1% of the initial catalytic active current, again suggesting the high operational durability. The remarkable catalytic stability was mainly ascribed to the intrinsic robustness of pyrite crystal phases and favorable gas transfer mechanism of nanoneedle arrays as well as the firm attachment between the SS support and the in-situ grown sulfide nanostructure.

### 2.3. Flexible Property

In addition to the aforementioned high bifunctional electrocatalytic performance, the mechanical flexibility of the SS mesh and the structural integrity of in-situ growth feature allowed the artificial bending of the prepared catalytic electrodes (Figure 7a). As can be seen from Figure 7b, to achieve a current density of 100 mA cm$^{-2}$, the resultant $Ni_{0.33}Co_{0.67}S_2$ NN/SS electrode rendered remarkable flexibility with an HER activity decay of only 10%, even after blending at 180° in alkaline media. As for OER electrocatalysis, we investigated the OER performance of the $Ni_{0.33}Co_{0.67}S_2$ NN/SS electrode after different bending times. Numerous gas bubbles were observed at a large current density of 300 mA cm$^{-2}$ on different bended electrodes (Figure 7c). More specially, the collected OER polarization curves were almost coincident after bending 20 and 40 times, respectively, as compared to the initial state without bending (Figure 7d). These observations highlight the remarkable performance of as-synthesized Ni–Co–S nanoneedle arrays on the SS as a flexible electrocatalytic electrode. The highly flexible and integrated electrode is promising for the future development of various flexible systems and devices, such as flexible fuel cells, metal–air batteries, portable hydrogen/oxygen fuel devices, and flexible photo-electrodes for photo-electrochemical catalysis and so on.
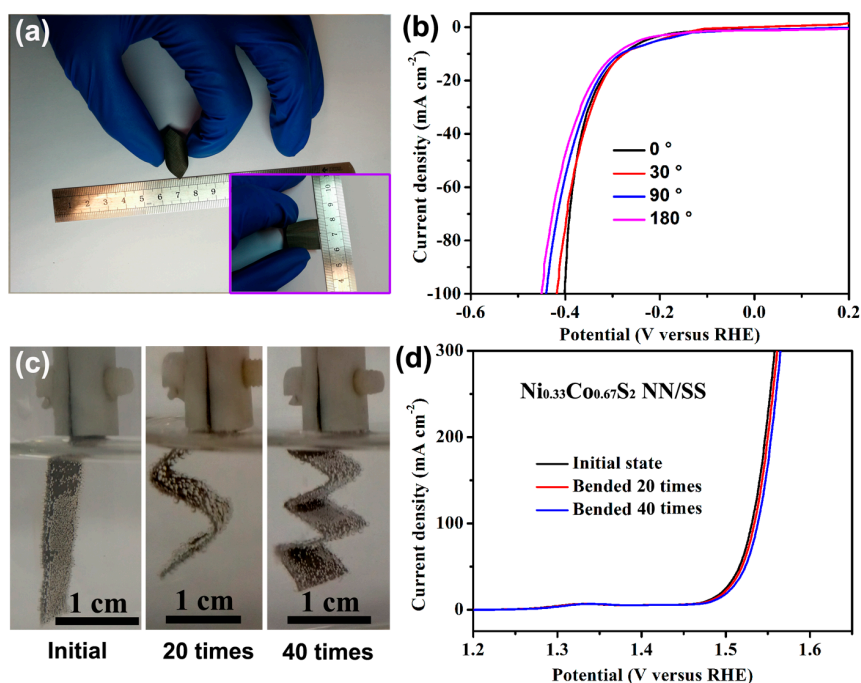


**Figure 7.** (**a**) Photograph of the flexible $Ni_{0.33}Co_{0.67}S_2$ NN/SS electrode at bended states. The inset shows the normal state; (**b**) HER polarization curves of $Ni_{0.33}Co_{0.67}S_2$ NN/SS electrodes at different bending angles; (**c**) Oxygen evolution images of $Ni_{0.33}Co_{0.67}S_2$ NN/SS electrodes at the initial state and after bending 20 and 40 times with an OER current density of 300 mA cm$^{-2}$; (**d**) OER polarization curves of $Ni_{0.33}Co_{0.67}S_2$ NN/SS electrodes after different bending times.

## 2.4. Overall Water-Splitting

Encouraged by the considerable electrochemical activity in promoting half reactions, $Ni_{0.33}Co_{0.67}S_2$ NN/SS was expected to act as a bifunctional electrode, serving as both a cathode for HER and an anode for OER in overall water splitting. As displayed in Figure 8a, the $Ni_{0.33}Co_{0.67}S_2$ NN/SS electrode is capable of catalyzing OER with anodic potential upon 1.23 V and is active for HER with a cathodic potential below 0 V. The fabricated $Ni_{0.33}Co_{0.67}S_2$ NN/SS ‖ $Ni_{0.33}Co_{0.67}S_2$ NN/SS electrolyzer afforded a current density of 10 mA cm$^{-2}$ at the required cell potential of 1.67 V (Figure 8b), which is only 110 mV higher than that of the Pt/C ‖ RuO$_2$–based electrochemical system. The combined overpotential of 440 mV for overall water splitting made the $Ni_{0.33}Co_{0.67}S_2$ NN/SS one of the reported active bifunctional catalysts, including metal hydroxides, oxides, chalcogenides and phosphides (Table S3). Obvious hydrogen and oxygen bubbles were generated on the electrode surface during the testing process (Figure 8c), evidencing the favorable kinetics during the water oxidation catalytic process. In addition, the long-term stability of the $Ni_{0.33}Co_{0.67}S_2$ NN/SS water-splitting system was evaluated in a continuous polarization for 10 h at 1.70 V. The activity retention was 81.4% for the $Ni_{0.33}Co_{0.67}S_2$ NN/SS-based electrolyzer, which is much lower than that of Pt/C + RuO$_2$ (51.7%, Figure 8d), demonstrating the considerable long-term durability of the $Ni_{0.33}Co_{0.67}S_2$ NN/SS electrode as both a cathode and anode electrode, in electrically catalyzing overall water splitting.



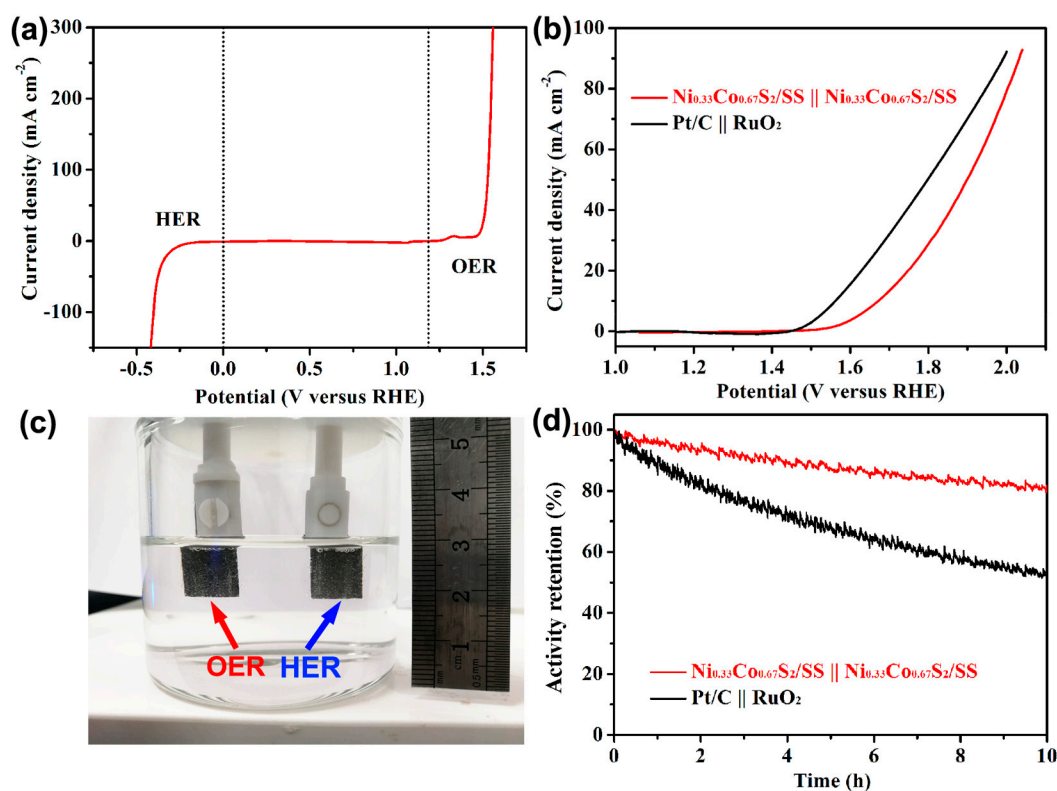**Figure 8.** (**a**) Polarization curve of $Ni_{0.33}Co_{0.67}S_2$ NN/SS, collected in a three-electrode configuration, with the potential ranging from −0.4 to 1.6 V; (**b**) Overall water-splitting performance tested by a two-electrode configuration in 1.0 M KOH; (**c**) Image of the H$_2$ and O$_2$ gas evolution on $Ni_{0.33}Co_{0.67}S_2$ NN/SS electrodes. The size of both the electrodes is 1 cm × 1 cm; (**d**) Long-term catalytic stability of fabricated electrolyzers at a fixed potential of 1.7 V.

## 3. Discussion

The electrochemical parameters of investigated catalysts are summarized in Table 1. Given that the catalytic performance is generally influenced by electronic and geometric factors, further consideration

is required to gain a deeper understanding about the influence of Ni component in $Ni_xCo_{1-x}S_2$ composite. As previous reported and based on our observations here (Figure 2), the doping of Ni into $CoS_2$ leads to a decrease in the geometric size of nanoneedles [43,44], improving the surface roughness and specific surface area (geometric effect). However, this trend is inconsistent with that observed in electrocatalytic performance ($Ni_{0.33}Co_{0.67}S_2$ > $Ni_{0.5}Co_{0.5}S_2$ > $Ni_{0.67}Co_{0.33}S_2$ > $CoS_2$), either in HER or OER. We next considered the effect from the electronic structure. On one hand, conductivity investigations on a series of spinel $Ni_xCo_{3-x}O_4$ ($0 \leq x \leq 1$) revealed that the activation energy almost disappears completely at a modest $x$ value, rendering the oxide with a semi-metallic nature [48,55]. On the other hand, the larger crystallite size may also result in a more conductive sample [48]. Thus, in our study, the $Ni_{0.33}Co_{0.67}S_2$ sample may have possessed the highest electrical conductivity in the $Ni_xCo_{1-x}S_2$ series, which facilitated the electron transfer during the catalytic reaction and allowed the superior catalytic activity toward both HER and OER. Actually, the optimized electron transfer at a moderate addition of Ni atoms into $CoS_2$ has been already revealed in literature [42], and is also corroborated by the EIS analysis, whereby the $Ni_{0.33}Co_{0.67}S_2$ exhibits the lowest charge transfer resistance among all studied compounds herein (Figure 5c). Otherwise, as revealed by the characterization of the electrochemical active surface area (Figure 6c), the catalytic active sites should also play a pivotal role in determining the catalytic performance. In the series of Ni-doped $CoS_2$, the Co-rich sample exhibited the highest overall activity, an indication that cobalt may energetically act as active sites for electrocatalysis to benefit the reaction kinetics, which is more effective than nickel sites [14]. Therefore, the superior performance of $Ni_{0.33}Co_{0.67}S_2$ could be attributed to the synergistic effect between the engineered electro-conductivity and the surface catalytic active sites, which simultaneously favors the electron transfer and facilitates the chemisorptions of hydrogen and oxygen-containing species, thus enhancing the overall electrocatalytic water-splitting activity.

**Table 1.** Summary of the electrochemical activities of $Ni_xCo_{1-x}S_2$ NN/SS electrodes with different Ni/Co ratios.

| Catalysts | Reaction | Tafel Slope (mV dec$^{-1}$) | Overpotential (mV) HER@30 mA cm$^{-2}$ OER@50 mA cm$^{-2}$ | $R_{ct}$ (Ω) | $C_{dl}$ (mF cm$^{-2}$) |
|---|---|---|---|---|---|
| $CoS_2$ | HER | 98 | 410 | 7.2 | |
| | OER | 99 | 340 | | |
| $Ni_{0.33}Co_{0.67}S_2$ | HER | 76 | 350 | 3.3 | 24.1 |
| | OER | 55 | 286 | | |
| $Ni_{0.5}Co_{0.5}S_2$ | HER | 82 | 370 | 3.9 | 17.6 |
| | OER | 61 | 292 | | |
| $Ni_{0.67}Co_{0.33}S_2$ | HER | 89 | 387 | 4.5 | 9.5 |
| | OER | 68 | 297 | | |

## 4. Materials and Methods

### 4.1. Synthesis

The Ni–Co precursors were grown on stainless steel, using a simple hydrothermal method. In a typical synthesis, 0.482 g urea, 0.194 g $Ni(NO_3)_2 \cdot 6H_2O$ and 0.388 g $Co(NO_3)_2 \cdot 6H_2O$ were added into 40 mL deionized water and continuously stirred for at least 30 min to obtain a clear solution. After that, a piece of stainless steel (1 cm × 1 cm), which was previously washed by acetone and ethanol in turns for five minutes and dried at 60 °C overnight, was immersed into the above aqueous solution. This mixed solution was transferred into a Teflon-lined stainless autoclave with the volume of 50 mL. After being tightly locked, the autoclave was maintained at 120 °C for 10 h in an electric oven. After naturally cooling down to room temperature, the stainless steel, wrapped with homogeneously distributed Ni–Co–carbonate hydroxide nanoneedle arrays, was obtained after washing by deionized

water for several times. The other Ni–Co carbonate hydroxide precursors, with different Ni:Co ratios, were prepared through the similar procedures, except by changing the added molar ratios of $Ni(NO_3)_2·6H_2O$ and $Co(NO_3)_2·6H_2O$, respectively.

The as-prepared Ni–Co precursor on stainless steel was converted into the corresponding sulfide nanostructures by a second hydrothermal process. In detail, 100 mg $Na_2S$ powder was dissolved into 30 mL deionized water and stirred for 10 min to form a sulfide precursor solution. Afterwards, the stainless steel substrate attached by Ni–Co–carbonate hydroxide precursor was immersed into the solution. The above solution was transferred to a 50 mL autoclave and maintained at 120 °C for 3 h in an electric oven. After cooling down naturally, the $Ni_xCo_{1-x}S_2$ nanoneedle arrays grown on SS ($Ni_xCo_{1-x}S_2$ NN/SS) were removed from the solution, washed with ethanol and DI water and then dried overnight at 60 °C.

*4.2. Characterization*

The phase formation of synthesized $Ni_xCo_{1-x}S_2$ series compounds and their precursors were identified using powder X-ray diffractometer (XRD, Bruker D8 Advanced, Bremen, Germany) with Cu K$\alpha$ radiation. The micro-nano morphologies were characterized by scanning electron microscopy (SEM, s4800, 30 kV, Hitachi, Tokyo, Japan) and transmission electron microscopy (TEM, jem-2100f, 200 kV, JEOL, Tokyo, Japan) along with energy dispersive spectroscopy (EDS), respectively. In order to perform the TEM measurement, the $Ni_xCo_{1-x}S_2$ samples were detached from the SS support by ultrasonic treatment, dispersed in ethanol to from a homogeneous solution, and then dripped on the copper grid. X-ray photoelectron spectroscopy (XPS) was conducted to detect the surface chemical compositions and elemental oxidation states using a ESCALAB 250XI (Thermo-Fisher Scientific, Waltham, MA, USA) apparatus with Al as the exciting source.

*4.3. Electrochemical Tests*

Electrochemical tests were carried out on an IviumStat electrochemical workstation (Ivium Technologies, Eindhoven, The Netherlands) using a three-electrode system in $N_2$-saturated 1.0 M KOH solution. The synthesized catalysts supported on the SS substrate were used as the working electrode. The corresponding counter electrode and reference electrode are graphite rod and saturated calomel electrode (SCE), respectively. All the electrochemical measurements were performed in 1.0 M KOH electrolyte, which was saturated with high-purity $N_2$ (Air Product, purity 99.995%, HuanYu Company, Tianjin, China) for at least 30 min before each test and maintained under the inert atmosphere throughout the whole test. The OER and HER linear sweeping voltammetry (LSV) data was collected at a scanning rate of 5 mV s$^{-1}$. Before collecting the final data, the working electrodes were repeatedly cycled by cyclic voltammograms (CVs) until the stable curves were obtained. All the mentioned potentials in this work were converted with respect to the reversible hydrogen electrode (RHE) using the following calibration: $E_{vs\ RHE} = E_{vs\ SCE} + 1.067$ V in 1.0 M KOH. The electrochemical capacitance ($C_{dl}$) was measured, from 1.12 to 1.22 V, at different scan rates of 5, 8, 10, 15, 20 mV s$^{-1}$, respectively. Electrochemical impedance spectroscopy (EIS) was performed with the sweeping frequency from 10 kHz to 100 mHz. The obtained EIS curves were fitted by a simplified Randles circuit, in order to determine the values of charge transfer resistance ($R_{ct}$). The overall water-splitting performance was measured in a two-electrode configuration, using the same catalysts as the active materials of both anode and cathode electrodes.

## 5. Conclusions

In summary, we have demonstrated the successful synthesis of $Ni_xCo_{1-x}S_2$ nanoneedles on SS support with different Ni/Co elemental ratios ($0 \leq x \leq 1$) and the chemical composition-dependent HER and OER electrocatalytic activities. Compared to other counterparts, the $Ni_{0.33}Co_{0.67}S_2$ NN/SS electrode exhibited superior bifunctional HER and OER performances, including lower overpotentials (286 mV at 50 mA cm$^{-2}$ of OER and 350 mV at 30 mA cm$^{-2}$ of HER), larger evolution currents

and faster kinetics (Tafel slopes of 55 and 76 mV dec$^{-1}$ for OER and HER) as well as remarkable long-term durability (e.g., no obvious decay of continuous OER catalysis for 15,000 s). Furthermore, the $Ni_{0.33}Co_{0.67}S_2$ NN/SS electrode rendered considerable flexibility with HER activity decay of only 10%, even after blending at 180° in alkaline media. The accelerated overall water-splitting performance of $Ni_{0.33}Co_{0.67}S_2$ NN/SS is ascribed to the favorable balance between the engineered electro-conductivity and the exposure of electrocatalytic surface active sites as well as the beneficial gas transfer over nanoneedle arrays surface. Meanwhile, the conductive, flexible SS substrate and firmly attached in-situ integrated feature contribute to the flexibility and remarkable catalytic stability of nickel cobalt sulfide-based electrodes. This work establishes the $Ni_{0.33}Co_{0.67}S_2$ NN/SS as a promising bifunctional electrode for water electrolyzation and also demonstrates the element doping strategy as an effective way to regulate conductivity and atomic active sites for enhancing the hydrogen and oxygen electrocatalysis.

**Supplementary Materials:** The following are available online at www.mdpi.com/2073-4344/7/12/366/s1, Figure S1: SEM images of precursors, Figure S2: Low-magnification SEM, Figure S3: EDS spectra, Figure S4: Measurement of lattice distance, Figure S5: TEM and HRTEM images of $Ni_{0.5}Co_{0.5}S_2$ and $Ni_{0.67}Co_{0.33}S_2$, Figure S6: OER performance of monometallic $CoS_2$ and $NiS_2$, Figure S7: SEM images of Ni–Co–S NN after OER polarization for 15,000 s, Figure S8: HER performance of monometallic $CoS_2$ and $NiS_2$, Figure S9: $C_{dl}$ measurements, Table S1: 2θ degree of selected crystal planes in prepared samples, Table S2: Comparison of OER performances of $Ni_{0.33}Co_{0.67}S_2$ NN/SS with other reported non-noble metal OER electrocatalysts in 1.0 M KOH, Table S3: Comparison of overall water-splitting performances of $Ni_{0.33}Co_{0.67}S_2$ NN/SS with other reported non-noble metal electrocatalysts in 1.0 M KOH.

**Author Contributions:** G.H. and W.Z. performed the experiments, Y.D. and C.Z. analyzed the data, X.H. wrote the paper and W.H directed the work.

**Conflicts of Interest:** The authors declare no conflict of interest.

## References

1. Nocera, D.G. The Artificial Leaf. *Acc. Chem. Rev.* **2012**, *45*, 767–776. [CrossRef] [PubMed]
2. Morales-Guio, C.G.; Stern, L.-A.; Hu, X. Nanostructured hydrotreating catalysts for electrochemical hydrogen evolution. *Chem. Soc. Rev.* **2014**, *43*, 6555–6569. [CrossRef] [PubMed]
3. Cook, T.R.; Dogutan, D.K.; Reece, S.Y.; Surendranath, Y.; Teets, T.S.; Nocera, D.G. Solar Energy Supply and Storage for the Legacy and Nonlegacy Worlds. *Chem. Rev.* **2010**, *110*, 6474–6502. [CrossRef] [PubMed]
4. Zou, X.; Zhang, Y. Noble metal-free hydrogen evolution catalysts for water splitting. *Chem. Soc. Rev.* **2015**, *44*, 5148–5180. [CrossRef] [PubMed]
5. Han, X.P.; Cheng, F.Y.; Zhang, T.R.; Yang, J.G.; Hu, Y.X.; Chen, J. Hydrogenated uniform Pt clusters supported on porous $CaMnO_3$ as a bifunctional electrocatalyst for enhanced oxygen reduction and evolution. *Adv. Mater.* **2014**, *26*, 2047–2051. [CrossRef] [PubMed]
6. Tian, J.; Liu, Q.; Asiri, A.M.; Sun, X. Self-Supported Nanoporous Cobalt Phosphide Nanowire Arrays: An Efficient 3D Hydrogen-Evolving Cathode over the Wide Range of pH 0–14. *J. Am. Chem. Soc.* **2014**, *136*, 7587–7590. [CrossRef] [PubMed]
7. Lee, Y.; Suntivich, J.; May, K.J.; Perry, E.E.; Shao-Horn, Y. Synthesis and Activities of Rutile $IrO_2$ and $RuO_2$ Nanoparticles for Oxygen Evolution in Acid and Alkaline Solutions. *J. Phys. Chem. Lett.* **2012**, *3*, 399–404. [CrossRef] [PubMed]
8. Tang, C.; Wang, W.; Sun, A.; Qi, C.; Zhang, D.; Wu, Z.; Wang, D. Sulfur-Decorated Molybdenum Carbide Catalysts for Enhanced Hydrogen Evolution. *ACS Catal.* **2015**, *5*, 6956–6963. [CrossRef]
9. Liu, Y.P.; Yu, G.T.; Li, G.D.; Sun, Y.H.; Asefa, T.; Chen, W.; Zou, X.X. Coupling $Mo_2C$ with Nitrogen-Rich Nanocarbon Leads to Efficient Hydrogen-Evolution Electrocatalytic Sites. *Angew. Chem. Int. Ed.* **2015**, *54*, 10752–10757. [CrossRef] [PubMed]
10. Fan, X.; Peng, Z.; Ye, R.; Zhou, H.; Guo, X. $M_3C$ (M: Fe, Co, Ni) Nanocrystals Encased in Graphene Nanoribbons: An Active and Stable Bifunctional Electrocatalyst for Oxygen Reduction and Hydrogen Evolution Reactions. *ACS Nano* **2015**, *9*, 7407–7418. [CrossRef] [PubMed]

11. Yan, H.; Tian, C.; Wang, L.; Wu, A.; Meng, M.; Zhao, L.; Fu, H. Phosphorus-Modified Tungsten Nitride/Reduced Graphene Oxide as a High-Performance, Non-Noble-Metal Electrocatalyst for the Hydrogen Evolution Reaction. *Angew. Chem. Int. Ed.* **2015**, *54*, 6325–6329. [CrossRef] [PubMed]

12. Jia, X.; Zhao, Y.; Chen, G.; Shang, L.; Shi, R.; Kang, X.; Waterhouse, G.I.N.; Wu, L.-Z.; Tung, C.-H.; Zhang, T. Ni$_3$FeN Nanoparticles Derived from Ultrathin NiFe-Layered Double Hydroxide Nanosheets: An Efficient Overall Water Splitting Electrocatalyst. *Adv. Energy Mater.* **2016**, *6*, 1502585. [CrossRef]

13. Staszak-Jirkovsky, J.; Malliakas, C.D.; Lopes, P.P.; Danilovic, N.; Kota, S.S.; Chang, K.-C.; Genorio, B.; Strmcnik, D.; Stamenkovic, V.R.; Kanatzidis, M.G.; et al. Design of active and stable Co-Mo-S$_x$ chalcogels as pH-universal catalysts for the hydrogen evolution reaction. *Nat. Mater.* **2016**, *15*, 197–204. [CrossRef] [PubMed]

14. Faber, M.S.; Lukowski, M.A.; Ding, Q.; Kaiser, N.S.; Jin, S. Earth-abundant metal pyrites (FeS$_2$, CoS$_2$, NiS$_2$, and their alloys) for highly efficient hydrogen evolution and polysulfide reduction electrocatalysis. *J. Phys. Chem. C* **2014**, *118*, 21347–21356. [CrossRef] [PubMed]

15. Ramakrishna, S. Cobalt sulfide nanosheet/graphene/carbon nanotube nanocomposites as flexible electrodes for hydrogen evolution. *Angew. Chem. Int. Ed.* **2014**, *53*, 12594–12599.

16. Wu, X.Y.; Han, X.P.; Ma, X.Y.; Zhang, W.; Deng, Y.D.; Zhong, C.; Hu, W.B. Morphology-Controllable Synthesis of Zn-Co-Mixed Sulfide Nanostructures on Carbon Fiber Paper Toward Efficient Rechargeable Zinc-Air Batteries and Water Electrolysis. *ACS Appl. Mater. Interfaces* **2017**, *9*, 12574–12583. [CrossRef] [PubMed]

17. Kong, D.; Wang, H.; Lu, Z.; Cui, Y. CoSe$_2$ Nanoparticles Grown on Carbon Fiber Paper: An Efficient and Stable Electrocatalyst for Hydrogen Evolution Reaction. *J. Am. Chem. Soc.* **2014**, *136*, 4897–4900. [CrossRef] [PubMed]

18. Zhang, H.; Yang, B.; Wu, X.; Li, Z.; Lei, L.; Zhang, X. Polymorphic CoSe$_2$ with Mixed Orthorhombic and Cubic Phases for Highly Efficient Hydrogen Evolution Reaction. *ACS Appl. Mater. Interfaces* **2015**, *7*, 1772–1779. [CrossRef] [PubMed]

19. Caban-Acevedo, M.; Stone, M.L.; Schmidt, J.R.; Thomas, J.G.; Ding, Q.; Chang, H.C.; Tsai, M.L.; He, J.H.; Jin, S. Efficient hydrogen evolution catalysis using ternary pyrite-type cobalt phosphosulphide. *Nat. Mater.* **2015**, *14*, 1245–1251. [CrossRef] [PubMed]

20. Duan, J.; Chen, S.; Vasileff, A.; Qiao, S.Z. Anion and Cation Modulation in Metal Compounds for Bifunctional Overall Water Splitting. *ACS Nano* **2016**, *10*, 8738–8745. [CrossRef] [PubMed]

21. Yang, H.C.; Zhang, Y.J.; Hu, F.; Wang, Q.B. Urchin-like CoP nanocrystals as hydrogen evolution reaction and oxygen reduction reaction dual-electrocatalyst with superior stability. *Nano Lett.* **2015**, *15*, 7616–7620. [CrossRef] [PubMed]

22. Wu, Y.; Liu, Y.; Li, G.-D.; Zou, X.; Lian, X.; Wang, D.; Sun, L.; Asefa, T.; Zou, X. Efficient electrocatalysis of overall water splitting by ultrasmall Ni$_x$Co$_{3-x}$S$_4$ coupled Ni$_3$S$_2$ nanosheet arrays. *Nano Energy* **2017**, *35*, 161–170. [CrossRef]

23. Wang, D.-Y.; Gong, M.; Chou, H.-L.; Pan, C.-J.; Chen, H.-A.; Wu, Y.; Lin, M.-C.; Guan, M.; Yang, J.; Chen, C.-W.; et al. Highly Active and Stable Hybrid Catalyst of Cobalt-Doped FeS$_2$ Nanosheets-Carbon Nanotubes for Hydrogen Evolution Reaction. *J. Am. Chem. Soc.* **2015**, *137*, 1587–1592. [CrossRef] [PubMed]

24. Zhu, H.; Zhang, J.; Yanzhang, R.; Du, M.; Wang, Q.; Gao, G.; Wu, J.; Wu, G.; Zhang, M.; Liu, B.; et al. When Cubic Cobalt Sulfide Meets Layered Molybdenum Disulfide: A Core-Shell System Toward Synergetic Electrocatalytic Water Splitting. *Adv. Mater.* **2015**, *27*, 4752–4759. [CrossRef] [PubMed]

25. Ji, D.; Peng, S.; Safanama, D.; Yu, H.; Li, L.; Yang, G.; Qin, X.; Srinivasan, M.; Adams, S.; Ramakrishna, S. Design of 3-Dimensional Hierarchical Architectures of Carbon and Highly Active Transition Metals (Fe, Co, Ni) as Bifunctional Oxygen Catalysts for Hybrid Lithium-Air Batteries. *Chem. Mater.* **2017**, *29*, 1665–1675. [CrossRef]

26. Su, Y.; Zhu, Y.; Jiang, H.; Shen, J.; Yang, X.; Zou, W.; Chen, J.; Li, C. Cobalt nanoparticles embedded in N-doped carbon as an efficient bifunctional electrocatalyst for oxygen reduction and evolution reactions. *Nanoscale* **2014**, *6*, 15080–15089. [CrossRef] [PubMed]

27. Zhao, J.J.; Quan, X.; Chen, S.; Liu, Y.M.; Yu, H.T. Cobalt Nanoparticles Encapsulated in Porous Carbons Derived from Core-Shell ZIF67@ZIF8 as Efficient Electrocatalysts for Oxygen Evolution Reaction. *ACS Appl. Mater. Interfaces* **2017**, *9*, 28685–28694. [CrossRef] [PubMed]

28. Zhang, Y.; Xia, X.; Cao, X.; Zhang, B.; Tiep, N.H.; He, H.; Chen, S.; Huang, Y.; Fan, H.J. Ultrafine Metal Nanoparticles/N-Doped Porous Carbon Hybrids Coated on Carbon Fibers as Flexible and Binder-Free Water Splitting Catalysts. *Adv. Energy Mater.* **2017**, *7*, 1700220. [CrossRef]

29. Gong, M.; Li, Y.; Wang, H.; Liang, Y.; Wu, J.Z.; Zhou, J.; Wang, J.; Regier, T.; Wei, F.; Dai, H. An Advanced Ni–Fe Layered Double Hydroxide Electrocatalyst for Water Oxidation. *J. Am. Chem. Soc.* **2013**, *135*, 8452–8455. [CrossRef] [PubMed]

30. Yu, L.; Zhou, H.Q.; Sun, J.Y.; Qin, F.; Yu, F.; Bao, J.M.; Yu, Y.; Chen, S.; Ren, Z.F. Cu nanowires shelled with NiFe layered double hydroxide nanosheets as bifunctional electrocatalysts for overall water splitting. *Energy Environ. Sci.* **2017**, *10*, 1820–1827. [CrossRef]

31. Song, Z.S.; Han, X.P.; Deng, Y.D.; Zhao, N.Q.; Hu, W.B.; Zhong, C. Clarifying the Controversial Catalytic Performance of $Co(OH)_2$ and $Co_3O_4$ for Oxygen Reduction/Evolution Reactions Toward Efficient Zn-Air Batteries. *ACS Appl. Mater. Interfaces* **2017**, *9*, 22694–22703. [CrossRef] [PubMed]

32. Ma, T.Y.; Dai, S.; Jaroniec, M.; Qiao, S.Z. Metal-organic framework derived hybrid $Co_3O_4$-carbon porous nanowire arrays as reversible oxygen evolution electrodes. *J. Am. Chem. Soc.* **2014**, *136*, 13925–13931. [CrossRef] [PubMed]

33. Bao, J.; Zhang, X.; Fan, B.; Zhang, J.; Zhou, M.; Yang, W.; Hu, X.; Wang, H.; Pan, B.; Xie, Y. Ultrathin Spinel-Structured Nanosheets Rich in Oxygen Deficiencies for Enhanced Electrocatalytic Water Oxidation. *Angew. Chem. Int. Ed.* **2015**, *54*, 7399–7404. [CrossRef] [PubMed]

34. Dou, S.; Dong, C.-L.; Hu, Z.; Huang, Y.-C.; Chen, J.-L.; Tao, L.; Yan, D.; Chen, D.; Shen, S.; Chou, S.; et al. Atomic-Scale $CoO_x$ Species in Metal-Organic Frameworks for Oxygen Evolution Reaction. *Adv. Funct. Mater.* **2017**, *27*, 1702546. [CrossRef]

35. Wang, X.; Li, W.; Xiong, D.; Petrovykh, D.Y.; Liu, L. Bifunctional Nickel Phosphide Nanocatalysts Supported on Carbon Fiber Paper for Highly Efficient and Stable Overall Water Splitting. *Adv. Funct. Mater.* **2016**, *26*, 4067–4077. [CrossRef]

36. Faber, M.S.; Dziedzic, R.; Lukowski, M.A.; Kaiser, N.S.; Ding, Q.; Jin, S. High-performance electrocatalysis using metallic cobalt pyrite ($CoS_2$) micro- and nanostructures. *J. Am. Chem. Soc.* **2014**, *136*, 10053–10061. [CrossRef] [PubMed]

37. Han, X.P.; Wu, X.Y.; Zhong, C.; Deng, Y.D.; Zhao, N.Q.; Hu, W.B. $NiCo_2S_4$ nanocrystals anchored on nitrogen-doped carbon nanotubes as a highly efficient bifunctional electrocatalyst for rechargeable zinc-air batteries. *Nano Energy* **2017**, *31*, 541–550. [CrossRef]

38. Zhang, J.; Wang, T.; Pohl, D.; Rellinghaus, B.; Dong, R.; Liu, S.; Zhuang, X.; Feng, X. Interface Engineering of $MoS_2/Ni_3S_2$ Heterostructures for Highly Enhanced Electrochemical Overall-Water-Splitting Activity. *Angew. Chem. Int. Ed.* **2016**, *55*, 6702–6707. [CrossRef] [PubMed]

39. Zhang, K.; Park, M.; Zhou, L.M.; Lee, G.H.; Shin, J.; Hu, Z.; Chou, S.L.; Chen, J.; Kang, Y.M. Cobalt-Doped $FeS_2$ Nanospheres with Complete Solid Solubility as a High-Performance Anode Material for Sodium-Ion Batteries. *Angew. Chem. Int. Ed.* **2016**, *55*, 12822–12826. [CrossRef] [PubMed]

40. Liu, Q.; Jin, J.; Zhang, J. $NiCo_2S_4$@graphene as a Bifunctional Electrocatalyst for Oxygen Reduction and Evolution Reactions. *ACS Appl. Mater. Interfaces* **2013**, *5*, 5002–5008. [CrossRef] [PubMed]

41. Fominykh, K.; Chernev, P.; Zaharieva, I.; Sicklinger, J.; Stefanic, G.; Döblinger, M.; Müller, A.; Pokharel, A.; Böcklein, S.; Scheu, C.; et al. Iron-Doped Nickel Oxide Nanocrystals as Highly Efficient Electrocatalysts for Alkaline Water Splitting. *ACS Nano* **2015**, *9*, 5180–5188. [CrossRef] [PubMed]

42. Zhang, H.H.; Guan, B.; Gu, J.N.; Li, Y.; Ma, C.; Zhao, J.; Wang, T.Y.; Cheng, C.J. One-step synthesis of nickel cobalt sulphides particles: Tuning the composition for high performance supercapacitors. *RSC Adv.* **2016**, *6*, 58916–58924. [CrossRef]

43. Chen, H.C.; Jiang, J.J.; Zhao, Y.D.; Zhang, L.; Guo, D.Q.; Xia, D.D. One-pot synthesis of porous nickel cobalt sulphides: Tuning the composition for superior pseudocapacitance. *J. Mater. Chem. A* **2015**, *3*, 428–437. [CrossRef]

44. Cui, Y.; Zhou, C.W.; Li, X.Z.; Gao, Y.; Zhang, J. High performance electrocatalysis for hydrogen evolution reaction using nickel-doped $CoS_2$ nanostructures: Experimental and DFT insights. *Electrochim. Acta* **2017**, *228*, 428–435. [CrossRef]

45. Kong, D.; Cha, J.J.; Wang, H.; Lee, H.R.; Cui, Y. First-row transition metal dichalcogenide catalysts for hydrogen evolution reaction. *Energy Environ. Sci.* **2013**, *6*, 3553–3558. [CrossRef]

46. Chen, G.; Liaw, S.S.; Li, B.; Xu, Y.; Dunwell, M.; Deng, S.; Fan, H.; Luo, H. Microwave-assisted synthesis of hybrid $Co_xNi_{1-x}(OH)_2$ nanosheets: Tuning the composition for high performance supercapacitor. *J. Power Sources* **2014**, *251*, 338–343. [CrossRef]

47. Yang, G.; Zhong, H.; Liu, R.; Li, Y.; Zou, B. In Situ Aggregation of ZnSe Nanoparticles into Supraparticles: Shape Control and Doping Effects. *Langmuir* **2013**, *29*, 1970–1976. [CrossRef] [PubMed]

48. Lambert, T.N.; Vigil, J.A.; White, S.E.; Davis, D.J.; Limmer, S.J.; Burton, P.D.; Coker, E.N.; Beechem, T.E.; Brumbach, M.T. Electrodeposited $Ni_xCo_{3-x}O_4$ nanostructured films as bifunctional oxygen electrocatalysts. *Chem. Commun.* **2015**, *51*, 9511–9514. [CrossRef] [PubMed]

49. Wang, X.; Yan, C.; Sumboja, A.; Lee, P.S. High performance porous nickel cobalt oxide nanowires for asymmetric supercapacitor. *Nano Energy* **2014**, *3*, 119–126. [CrossRef]

50. Peng, Z.; Jia, D.S.; Al-Enizi, A.M.; Elzatahry, A.A.; Zheng, G.F. From Water Oxidation to Reduction: Homologous Ni-Co Based Nanowires as Complementary Water Splitting Electrocatalysts. *Adv. Energy Mater.* **2015**, *5*, 1402031. [CrossRef]

51. Vrubel, H.; Merki, D.; Hu, X. Hydrogen evolution catalyzed by $MoS_3$ and $MoS_2$ particles. *Energy Environ. Sci.* **2012**, *5*, 6136–6144. [CrossRef]

52. Chang, Y.-H.; Lin, C.-T.; Chen, T.-Y.; Hsu, C.-L.; Lee, Y.-H.; Zhang, W.; Wei, K.-H.; Li, L.-J. Highly Efficient Electrocatalytic Hydrogen Production by $MoS_x$ Grown on Graphene-Protected 3D Ni Foams. *Adv. Mater.* **2013**, *25*, 756–760. [CrossRef] [PubMed]

53. Xiao, J.; Wan, L.; Yang, S.; Xiao, F.; Wang, S. Design Hierarchical Electrodes with Highly Conductive $NiCo_2S_4$ Nanotube Arrays Grown on Carbon Fiber Paper for High-Performance Pseudocapacitors. *Nano Lett.* **2014**, *14*, 831–838. [CrossRef] [PubMed]

54. Sivanantham, A.; Ganesan, P.; Shanmugam, S. Hierarchical $NiCo_2S_4$ Nanowire Arrays Supported on Ni Foam: An Efficient and Durable Bifunctional Electrocatalyst for Oxygen and Hydrogen Evolution Reactions. *Adv. Funct. Mater.* **2016**, *26*, 4661–4672. [CrossRef]

55. Appandairajan, N.K.; Gopalakrishnan, J. A study of $Co_{3-x}Ni_xO_4$ ($O \leq x \leq 1$) system. *Proc. Indian Acad. Sci. Sect. A* **1978**, *87*, 115–120.